JMI Journal of Medical Imaging

RESEARCH PAPER

Charge-cloud-based micrometer resolution in deep-silicon photon-counting CT

Rickard Brunskog,[a,b,*] **Mats Persson**,[a,b] **Moa Yveborg Tamm**,[a,b] **Umberto Follo**,[c] and **Mats Danielsson**[a,b]
[a]KTH Royal Institute of Technology, Physics of Medical Imaging, Stockholm, Sweden
[b]Karolinska University Hospital, MedTechLabs, BioClinicum, Solna, Sweden
[c]Istituto Nazionale di Fisica Nucleare (INFN), Sezione di Torino, Turin, Italy

ABSTRACT. **Purpose:** We are developing a monolithic deep-silicon photon-counting sensor targeting spatial resolution on the order of 1 μm. This work investigates how pixel pitch, noise level, threshold number, and threshold placement affect the achievable tangential and wafer-thickness resolution to guide the CMOS electronics and sensor design.

Approach: Allpix Squared simulations were used to evaluate pixel pitches with two noise levels and two threshold-placement schemes over varying threshold numbers. Interaction position was estimated in both dimensions using lookup tables trained on the thresholded pixel output, and performance was quantified using the MTF.

Results: Decreasing pixel pitch strongly improved tangential resolution for Compton interactions, whereas photoelectric interactions showed a weaker dependence on pixel pitch and threshold placement. Equal-counting thresholds approached the achievable resolution with fewer thresholds than equidistant thresholds. For eight equal-counting thresholds, the 10% MTF across the studied pixel sizes ranged from 1284 lp/cm to 2452 lp/cm in the tangential direction and from 15 to 71 lp/cm in the wafer-thickness direction for Compton interactions, compared with 409 to 507 lp/cm and 18 to 79 lp/cm, respectively, for photoelectric interactions. RMSE analysis further showed that some interactions for the 25 μm pitch reached below 2 μm tangentially and a few tens of micrometers in the wafer-thickness direction.

Conclusions: Spatial resolution improved with a threshold number up to about 8 to 10, beyond which additional programmable thresholds gave only modest gain. The achieved tangential resolution also suggests that analyzer-free phase-contrast imaging is feasible for realistic geometries and expected interference patterns.

 [DOI: 10.1117/1.JMI.13.4.043501]

Keywords: computed tomography; deep-silicon detectors; edge-on sensors; photon-counting detectors; spatial resolution

Paper 260269 received May 20, 2026; revised Jul. 14, 2026; accepted Jul. 20, 2026; published Aug. 6, 2026.

1 Introduction

We are developing a detector capable of performing single-photon interaction readout using a monolithic deep-silicon photon-counting CMOS sensor. The design goal is an ultra-high-resolution, fully depleted, CMOS monolithic active pixel sensor (MAPS) based on the ARCADIA technology developed at the National Institute for Nuclear Physics (INFN, Italy).[1–3] An early experimental prototype of the high-resolution deep-silicon detector concept was previously

*Address all correspondence to Rickard Brunskog, rbru@kth.se

evaluated by Brunskog et al., where measured channel responses from a partially connected prototype sensor were compared with simulations to validate the detector model and demonstrate hardware feasibility.[4] Using a monolithic design, pixel pitches down to the order of 10 μm can be achieved, and the spread of the charge cloud can be leveraged to reach sub-pixel resolution. A potential application of such ultra-high resolution is analyzer-free phase-contrast imaging, where interference patterns can be on the order of a few tens of micrometers; for example, Viermetz et al. reported a fringe period of 45 μm on the detector.[5–10] A detector with sufficiently high spatial resolution could therefore eliminate the need for an analyzer grating, potentially making clinical implementation of phase-contrast more compact and practical.

In previous work by Sundberg et al., the pixel energies are read out without additional thresholding beyond the lowest threshold, and a Gaussian fit is used to estimate the tangential x-position from the fitted mean, while the fitted standard deviation is used to estimate the wafer-thickness y-position, thereby providing both sub-pixel-pitch and sub-wafer-thickness resolution.[11] Sub-pixel resolution has also been demonstrated in other detectors, such as the MÖNCH detector, albeit not in the energy range and count-rate regime of medical imaging CT.[12]

Building on the work by Sundberg et al., and extending beyond the early prototype validation by Brunskog et al., this study introduces two main changes.[4,11] First, it considers a thresholded readout, which is more closely related to a realistic CMOS implementation, rather than using pixel energies without additional thresholding beyond the lowest threshold. Second, instead of estimating the interaction position from a Gaussian fit to the charge cloud, a lookup table (LUT) is applied directly to the thresholded pixel output in both the tangential and wafer-thickness directions. This avoids the need for a computationally demanding fit for each interaction and provides a simpler reconstruction method for hardware implementation. The study further investigates how pixel pitch, noise level, number of thresholds, and threshold placement affect the information available for position reconstruction, with the aim of guiding the upcoming electronics and sensor design by identifying which threshold configuration can provide high resolution and enable analyzer-free phase-contrast imaging.

2 Materials and Methods

2.1 Sensor Geometry

We employ an edge-on configuration where each pixel pitch is simulated as a silicon wafer with a thickness of 650 μm and electrodes on the top surface, with 31 pixels along the tangential direction. A view of several edge-on sensor wafers, stacked into a module and interleaved with tungsten sheets to absorb scattered photons, can be seen in Fig. 1. Figure 1 also shows a sketch of the pixel geometry, as well as the definition of the tangential (x) and wafer-thickness (y) dimensions used in this work. Several sensor wafers can be stacked into a module, and multiple modules can then be assembled to cover the desired area, as seen in Fig. 2.

2.2 Allpix Squared Simulation

The simulation chain uses the Allpix Squared framework to model photon transport, photon interactions, charge-carrier propagation, and signal formation in the pixels. A 120 kVp X-ray

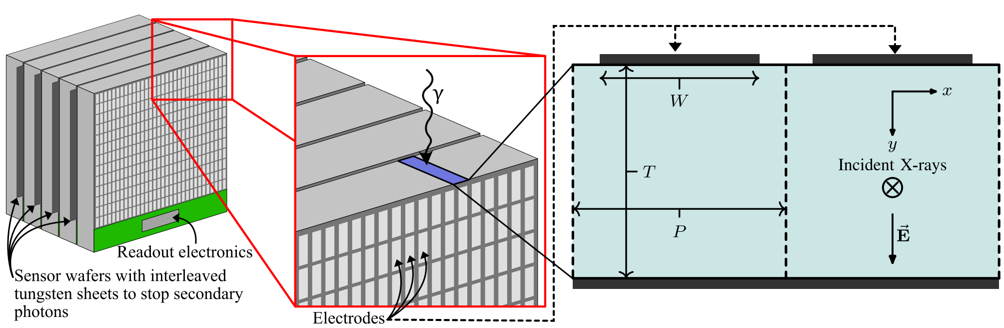

Fig. 1 Left: view of multiple stacked wafers, with interleaved tungsten sheets to stop scattered photons. Right: zoomed-in view of the edge-on geometry with pixel pitch P, wafer thickness T, and electrode width W.

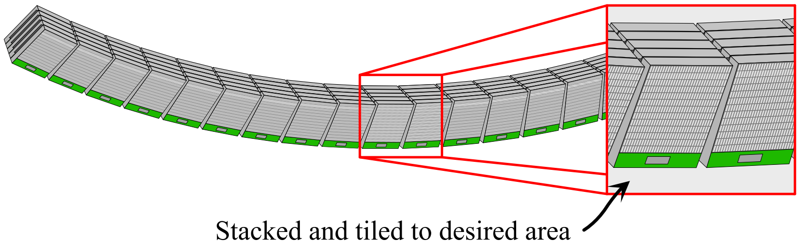

Fig. 2 Using the stacked wafer modules from Fig. 1, the detector can be built to cover the desired area.

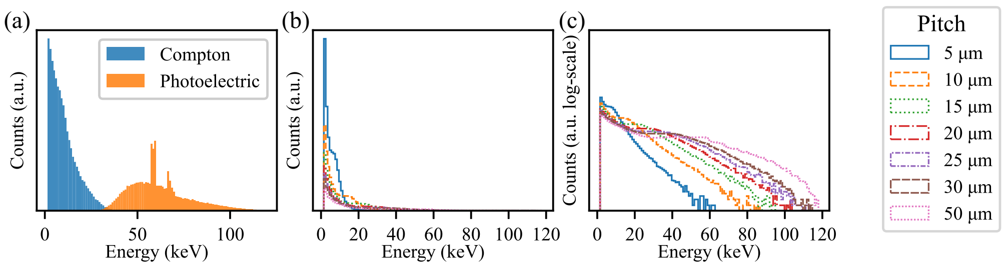

Fig. 3 (a) Deposited spectrum with Compton interactions and photoelectric interactions colored separately, (b) energy induced in the individual pixels, and (c) energy induced in the individual pixels on a logarithmic scale.

spectrum, filtered by 0.8 mm Be, 4 mm Al, and 300 mm water, is generated using SpekPy. The 300 mm water filtration was chosen to represent a clinically relevant adult-body attenuation condition while providing a fixed reference case for evaluating the detector-design parameters studied here. The photon energies are then sampled from the resulting histogram, and the corresponding deposited energies are shown in Fig. 3(a).[13–15] The photons are generated as a rectangular, spatially uniform beam that covers the full source-facing pixel area at the sensor edge and is incident perpendicularly on that surface, as shown in Fig. 1.

The electric field and the weighting potential used by Allpix Squared are simulated in COMSOL using the Electrostatics module and the Mathematics module, respectively.[16–18] Figure 4(a) shows the two-dimensional center-of-the-pixel electric potential with field streamlines, and Fig. 4(b) shows the weighting potential, both for the 25 µm pitch. The electric field is simulated for a silicon wafer with flat electrodes of width W on the surface, where W is given in Table 1.

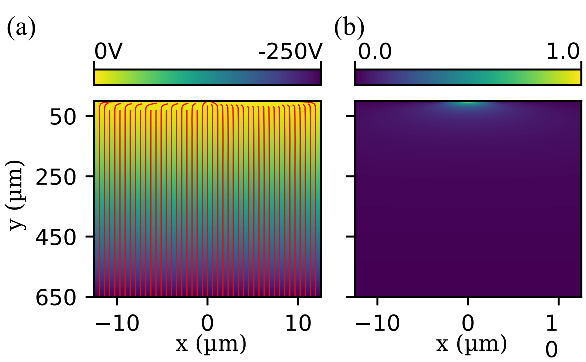

Fig. 4 (a) Electric potential with electric field streamlines for the 25 µm pitch, and (b) the weighting potential for the 25 µm pitch.

Table 1 Pixel geometry and threshold configurations for lowest thresholds of 1.5 keV and 0.5 keV.

P (μm)	W (μm)	T (μm)	Bias (V)	Lowest threshold at $4\sigma_E$ (keV)	Highest threshold (keV)	Max number of thresholds for 1.5 keV/0.5 keV
5	1	650	−250	1.5/0.5	12	8/26
10	1	650	−250	1.5/0.5	22	10/46
15	1	650	−250	1.5/0.5	31	15/64
20	1	650	−250	1.5/0.5	39	20/80
25	1	650	−250	1.5/0.5	45	25/92
30	3	650	−250	1.5/0.5	51	30/102
50	3	650	−250	1.5/0.5	63	50/126

Table 2 Key Allpix Squared simulation settings.

Category	Setting
Geant4	Physics list: `FTFP_BERT_PEN`; world: vacuum
Source	Photon primaries (`gamma`); spectrum via Geant4 macro
Bulk resistivity	Constant 15 kΩ cm
Transport module	`InteractivePropagation`; $T = 293$ K; mobility: Masetti–Canali; $\Delta t = 0.05$ ns; $t_{\mathrm{int}} = 100$ ns
Diffusion/recombination	Diffusion enabled; recombination: `srh_auger`
Coulomb repulsion	Enabled; distance limit: 200 μm; field limit: 400000 V/cm
Surface	Surface reflectivity: 1.0; mirror charges: off

The charge-carrier propagation is simulated with a custom propagation module called InteractivePropagation, which, in addition to diffusion, also implements the Coulomb force between charge carriers.[19] The signal is then transferred to the electrodes using the PulseTransfer module, and digitization is performed in postprocessing. Key settings are summarized in Table 2. To isolate the intrinsic localization performance, only primary interactions are considered in this work. Multiinteraction events are expected to alter the PSF, MTF, and RMSE and likely reduce the localization accuracy. Quantifying both the occurrence rate and the impact of such events under realistic spectra and detector geometries was outside the scope of the present study and is left for future work.

2.3 Energy Thresholds and Signal Noise

From the Allpix Squared output, the true x-position, true y-position, and ideal pixel energies are extracted for each interaction. The thresholding is then studied using two placement schemes: equidistant thresholds and equal-count quantiles of the per-pixel induced-energy distribution in Figs. 3(b) and 3(c). Two noise levels, $\sigma_{E,1} = 0.375$ keV and $\sigma_{E,2} = 0.125$ keV, are considered. These were chosen as representative design-point assumptions based on experience from earlier ARCADIA sensors, with 0.375 keV taken as a realistic baseline and 0.125 keV as an optimistic cooled-detector case, rather than as values from a specific measured ASIC. The corresponding lowest thresholds are set to $4\sigma_{E,i}$, whereas the highest threshold is chosen such that 5% of the counts in Figs. 3(b) and 3(c) lie above it. The minimum threshold separation is set equal to the lowest threshold in each case, i.e., $\Delta E_{\mathrm{min},1} = 1.5$ keV and $\Delta E_{\mathrm{min},2} = 0.5$ keV. In the limiting case of minimum threshold spacing, this corresponds to about 20% bin misclassifications due to noise. Table 1 summarizes the pixel geometries and threshold configurations. Because of the minimum-threshold-separation constraint, the two placement schemes become increasingly similar as the number of thresholds increases, and are identical at the maximum number of thresholds.

2.4 Variable Estimation

To estimate the interaction position from the thresholded pixel response, a lookup table (LUT) is used. The LUT provides a computationally simple alternative to event-by-event fitting by learning, from simulated training data, the mapping between thresholded pixel-response patterns and the corresponding interaction position. In practice, each unique thresholded pixel cluster is treated as a discrete state, and the LUT stores the representative position associated with that state. The LUT is trained on one dataset and evaluated on a separate dataset, with each dataset containing ~100,000 Compton interactions and 50,000 photoelectric interactions.

2.4.1 *x-position*

The LUT takes the processed pixel vector after noise and thresholding,

$$\mathbf{q} = (q_1, q_2, \dots, q_N), \tag{1}$$

where q_i is the thresholded energy value in pixel i, and N is the total number of pixels in the simulation. The LUT then identifies the contiguous cluster of triggered pixels and is built using keys of the form

$$\mathbf{s} = (q_l, q_{l+1}, \dots, q_{r-1}, q_r), \tag{2}$$

with r and l denoting the rightmost and leftmost triggered pixel indices, respectively.

The reference position is defined as

$$x_{\text{ref}} = \frac{x_l + x_r}{2}, \tag{3}$$

where x_l and x_r are the physical positions of the leftmost and rightmost triggered pixels. The LUT is then trained on the position relative to the cluster center according to

$$u_x = x^{\text{true}} - x_{\text{ref}}, \tag{4}$$

thus learning the mapping

$$\mathbf{s} \to u_x, \tag{5}$$

and the estimated x-position is obtained as

$$\hat{x} = x_{\text{ref}} + \text{LUT}_x(\mathbf{s}). \tag{6}$$

During training, a unique key has multiple targets $(u_1, \dots, u_k)$, and the median of these values is stored as the estimate for that key according to

$$\text{LUT}_x(\mathbf{s}) = \text{median}(u_1, \dots, u_k). \tag{7}$$

If the input to the LUT after training is unknown, the nearest state is used as a fallback, calculated using the L_1 distance in feature space.

2.4.2 *y-position*

For the y-position, the LUT is trained on the same keys as for the x-position, but learns the absolute mapping instead of the local mapping, i.e.,

$$\mathbf{s} \to y^{\text{true}}. \tag{8}$$

Similar to the x-position, the median of the true y-positions of the training data is stored as the estimate for that key, given by

$$\hat{y} = \text{LUT}_y(\mathbf{s}) = \text{median}(y_1^{\text{true}}, \dots, y_k^{\text{true}}). \tag{9}$$

If the input to the LUT after training is unknown, the nearest state is used as a fallback, again based on the L_1 distance in feature space.

2.5 Measure of Performance

For each photon interaction i, the error between the estimated and true interaction position is calculated according to

$$\Delta x_i = \hat{x}_i - x_i^{\text{true}}, \tag{10}$$

and

$$\Delta y_i = \hat{y}_i - y_i^{\text{true}}. \tag{11}$$

The point spread function (PSF) for each dimension is then taken as the normalized histogram of the error of the respective coordinate. The PSFs for both x and y are sampled on a uniform grid, with the histogram bin width selected adaptively using a Freedman–Diaconis bin-width rule with 0.25σ as a bin-width fallback, where σ is the standard deviation of the errors.[20,21] The modulation transfer function (MTF) is computed as the magnitude of the Fourier transform of the PSF, and the chosen metric is the 10% MTF value for the x- and y-resolution as a function of the number of thresholds, with the interactions separated into lower-energy Compton interactions, higher-energy photoelectric interactions, and both combined.

3 Results & Discussion

The detection efficiency of the sensor at low energies depends on the lowest threshold, and for sufficiently small pixel pitches, the interactions that would otherwise be detected may fall below that threshold due to the charge-cloud spread. Figures 5(a)–5(g) show the number of contiguous pixels with induced energy above the lowest threshold for 5 μm to 50 μm, for lowest thresholds of 1.5 and 0.5 keV. With the lowest threshold at 1.5 keV, there is an increase in undetected interactions once the pixel pitch becomes smaller than about 15 μm, which suggests that to make practical use of the smallest pixel sizes, the noise needs to be lowered significantly. For pixel sizes of 15 μm and above, the number of missed interactions decreases slowly with increasing pixel pitch, but the spread distribution shifts progressively toward 1- and 2-pixel clusters.

Figures 6 and 7 show the 10% MTF values as a function of the number of thresholds for the 1.5 keV lowest-threshold case with equidistant and equal-counting thresholds, respectively, while Figs. 8 and 9 show the corresponding results for the 0.5 keV case. Panels (a)–(c) show the x-resolution for Compton interactions, photoelectric interactions, and both interaction types combined, respectively, whereas panels (d)–(f) show the corresponding y-resolution.

For the x-resolution, in the 1.5 keV lowest threshold case, the Compton interactions show a strong dependence on threshold placement. In Figs. 6 and 7, the maximum resolution of the equidistant thresholds is reached only at the maximum number of thresholds, whereas the same limiting resolution is reached with significantly fewer equal-counting thresholds. The same overall behavior is seen for the 0.5 keV case in Figs. 8 and 9, although the smaller pixel sizes benefit more from the lower noise than the larger pixel sizes. In contrast, the photoelectric interactions in panels (b) show a much weaker dependence on threshold placement, and both lowest-threshold

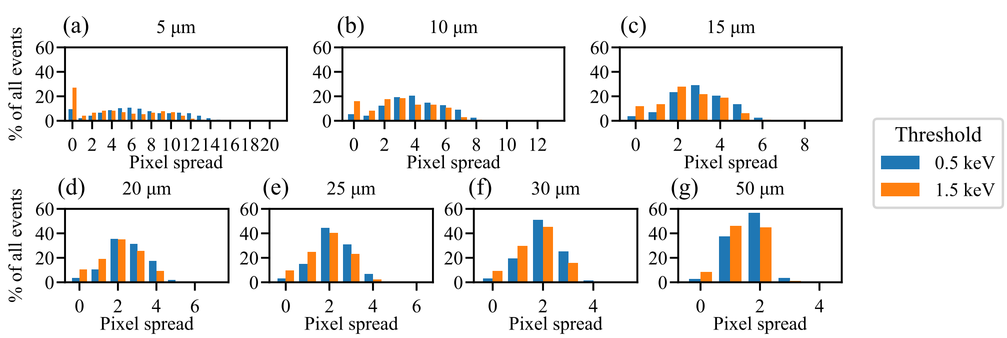

Fig. 5 Histogram of the number of contiguous pixels for which the charge-carrier cloud from a single photon interaction induces an energy above the lowest threshold for (a) 5 μm pitch, (b) 10 μm pitch, (c) 15 μm pitch, (d) 20 μm pitch, (e) 25 μm pitch, (f) 30 μm pitch, and (g) 50 μm pitch, with 0 pixel spread indicating undetected interactions.

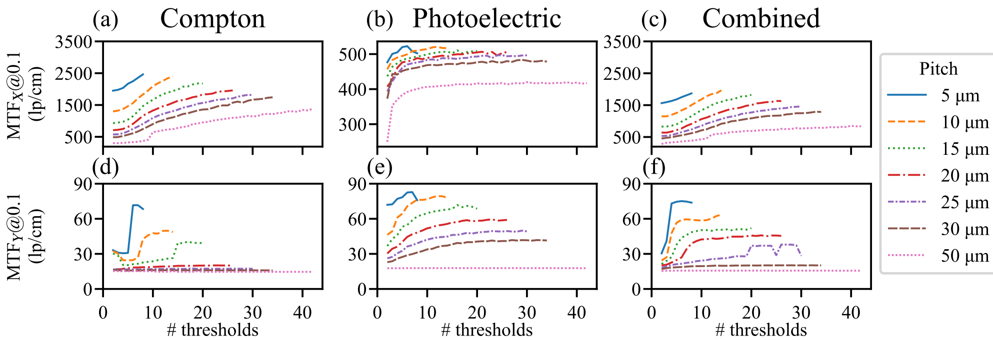

Fig. 6 Panels (a)–(c) show the 10% *x*-MTFs for Compton interactions, photoelectric interactions, and both interaction types combined, respectively, for the 1.5 keV lowest-threshold case with equidistant thresholds. Panels (d)–(f) show the corresponding 10% *y*-MTFs.

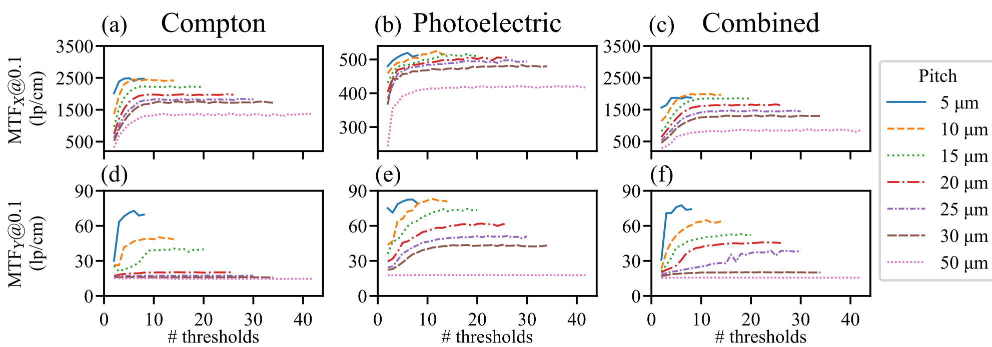

Fig. 7 Panels (a)–(c) show the 10% *x*-MTFs for Compton interactions, photoelectric interactions, and both interaction types combined, respectively, for the 1.5 keV lowest-threshold case with equal-counting thresholds. Panels (d)–(f) show the corresponding 10% *y*-MTFs.

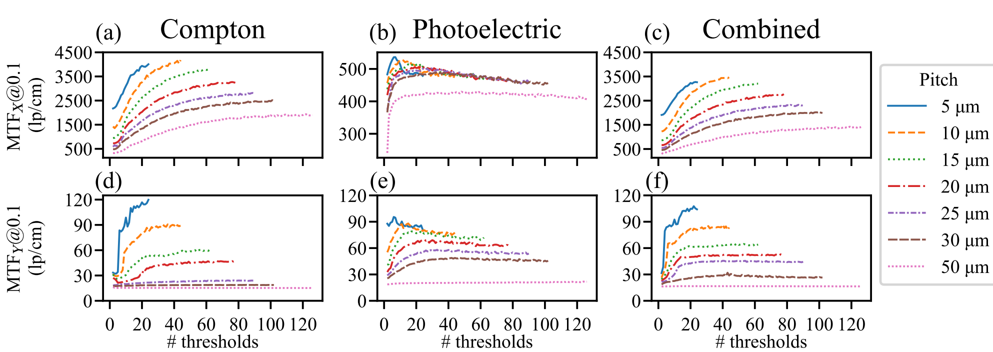

Fig. 8 Panels (a)–(c) show the 10% *x*-MTFs for Compton interactions, photoelectric interactions, and both interaction types combined, respectively, for the 0.5 keV case with equidistant thresholds. Panels (d)–(f) show the corresponding 10% *y*-MTFs.

cases show that their resolution reaches a maximum before slowly decreasing. This, together with the narrow spread of the 10% MTF curves and the very similar performance of the 5 and 10 μm pixel pitches, suggests that the longer electron tracks at higher energies introduce a fundamental uncertainty in the position estimate, while the decrease at large threshold numbers most likely stems from increased bin misclassifications as the threshold spacing becomes narrower. Taken together, this indicates that for the two noise and threshold configurations considered here, the limiting resolution of each pixel pitch can be approached using significantly fewer thresholds by applying the equal-counting thresholds rather than the equidistant scheme, particularly for the Compton *x*-resolution.

For the *y*-resolution in the 1.5 keV case, Figs. 6(d) and 7(d) show negligible improvement for the Compton interactions when going from 50 to 20 μm, with larger improvements only

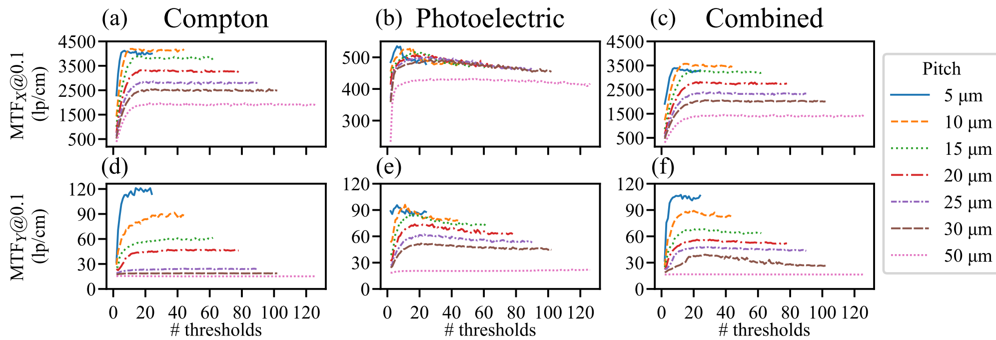

Fig. 9 Panels (a)–(c) show the 10% x-MTFs for Compton interactions, photoelectric interactions, and both interaction types combined, respectively, for the 0.5 keV case with equal-counting thresholds. Panels (d)–(f) show the corresponding 10% y-MTFs.

appearing for the smallest pixel sizes, whereas the photoelectric interactions in Figs. 6(e) and 7(e) already improve at pixel pitches of 30 μm. The resolution using equal-counting thresholds again shows a faster increase with the number of thresholds for the smaller pixel sizes, but the threshold-placement scheme has little effect for pixel sizes of 20 μm and larger. The same overall behavior is seen for the 0.5 keV case in Figs. 8 and 9, although the resolution of the Compton interactions improves more strongly with the number of thresholds for pixel sizes of 20 μm and below, while the photoelectric interactions show a more moderate increase. For the 50 μm pixel size, there is minimal improvement for either threshold-placement scheme, indicating a limit to the achievable y-resolution for pixel sizes larger than about 30 μm.

Figures 10 and 11 show the PSFs and MTFs, respectively, for 8 equal-counting thresholds and a lowest threshold of 1.5 keV, whereas Figs. 12 and 13 show the corresponding results for the

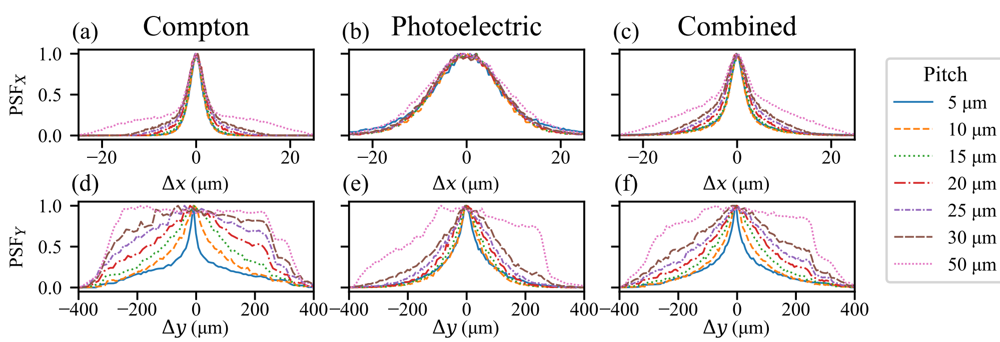

Fig. 10 Panels (a)–(c) show the x-PSFs for Compton interactions, photoelectric interactions, and both interaction types combined, respectively, for the 1.5 keV lowest-threshold case with eight equal-counting thresholds for all pitch sizes. Panels (d)–(f) show the corresponding y-PSFs.

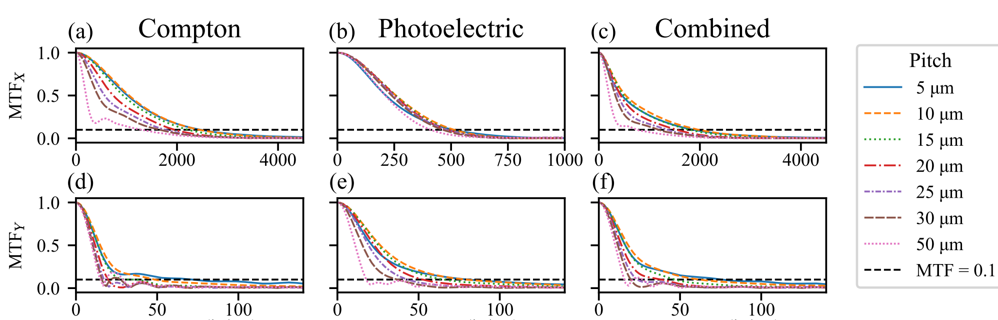

Fig. 11 Panels (a)–(c) show the x-MTFs for Compton interactions, photoelectric interactions, and both interaction types combined, respectively, for the 1.5 keV lowest-threshold case with eight equal-counting thresholds for all pitch sizes. Panels (d)–(f) show the corresponding y-MTFs.

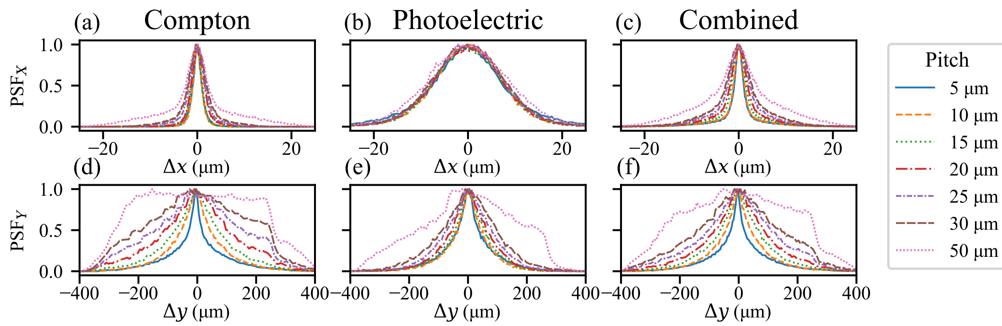

Fig. 12 Panels (a)–(c) show the *x*-PSFs for Compton interactions, photoelectric interactions, and both interaction types combined, respectively, for the 0.5 keV case with eight equal-counting thresholds for all pitch sizes. Panels (d)–(f) show the corresponding *y*-PSFs.

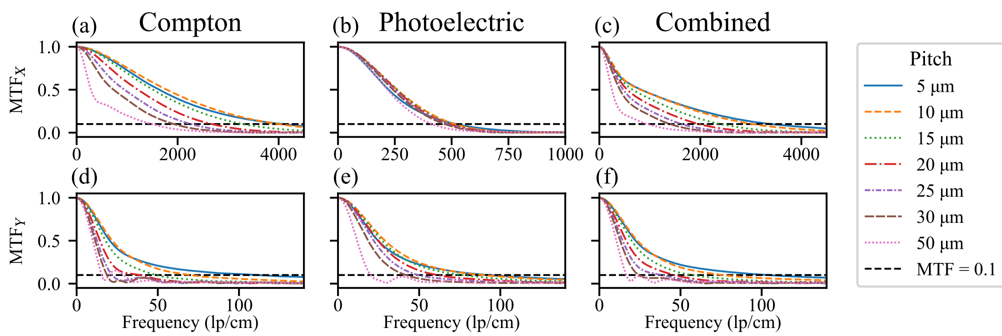

Fig. 13 Panels (a)–(c) show the *x*-MTFs for Compton interactions, photoelectric interactions, and both interaction types combined, respectively, for the 0.5 keV case with eight equal-counting thresholds for all pitch sizes. Panels (d)–(f) show the corresponding *y*-MTFs.

0.5 keV case. The corresponding FWHM and 10% MTF values are listed in Tables 3–6, and Fig. 14 shows the 10% MTF values as a function of the true total deposited energy in the sensor.

For the *x*-resolution at eight equal-counting thresholds, Figs. 10(a) and 11(a) show that in the 1.5 keV lowest-threshold case, the pixel pitches of 5 to 15 μm have very similar PSFs and MTFs, whereas the larger pixel pitches degrade in performance, with the 50 μm pixel pitch performing significantly worse. The photoelectric interactions in panels (b) again show the limiting effect of the electron track on the resolution, with all pixel pitches performing essentially the same. The observations for the 1.5 keV case largely hold for the 0.5 keV case in Figs. 12 and 13, although here the 5 and 10 μm slightly outperform the 15 μm.

Table 3 Metrics at $N_{thr} = 8$ for 1.5 keV lowest threshold (equal-counting thresholds), for Compton interactions.

Pitch (μm)	$FWHM_X$ (μm)	MTF_X@0.1 (lp/cm)	FWHM (μm)	MTF_Y@0.1 (lp/cm)
5	3.3	2452	41	71
10	3.2	2405	128	49
15	3.5	2199	225	31
20	4.0	1978	408	20
25	4.3	1777	508	17
30	4.6	1665	545	16
50	5.1	1284	613	15

Table 4 Metrics at $N_{thr} = 8$ for 1.5 keV lowest threshold (equal-counting thresholds), for photoelectric interactions.

Pitch (μm)	$FWHM_X$ (μm)	MTF_X@0.1 (lp/cm)	FWHM (μm)	MTF_Y@0.1 (lp/cm)
5	16.0	502	76	79
10	15.3	507	89	77
15	16.1	492	107	65
20	16.7	480	144	52
25	16.1	480	180	44
30	17.3	464	214	37
50	19.4	409	475	18

Table 5 Metrics at $N_{thr} = 8$ for the lowest threshold 0.5 keV (equal-counting thresholds), for Compton interactions.

Pitch (μm)	$FWHM_X$ (μm)	MTF_X@0.1 (lp/cm)	FWHM (μm)	MTF_Y@0.1 (lp/cm)
5	1.9	4079	42	114
10	1.9	3987	96	70
15	2.4	3261	148	49
20	2.9	2649	204	39
25	3.6	2203	307	22
30	4.0	1937	460	19
50	4.9	1485	546	16

Table 6 Metrics at $N_{thr} = 8$ for the lowest threshold 0.5 keV (equal-counting thresholds), for photoelectric interactions.

Pitch (μm)	$FWHM_X$ (μm)	MTF_X@0.1 (lp/cm)	FWHM (μm)	MTF_Y@0.1 (lp/cm)
5	15.4	513	75	91
10	15.4	512	80	89
15	15.7	496	102	75
20	16.5	486	118	61
25	16.7	478	152	49
30	17.5	470	182	42
50	18.5	413	420	20

The y-resolution at eight thresholds for the 1.5 keV case in Figs. 10(d) and 11(d) shows that for a significant improvement in the wafer-thickness direction for the Compton interactions to be seen, a pixel pitch of 15 μm or smaller is needed. For the 0.5 keV case in Figs. 12(d) and 13(d), the same improvement is seen for pixel pitches of 20 μm and below. The photoelectric interactions in panel (e) indicate that more information about wafer-thickness localization is available

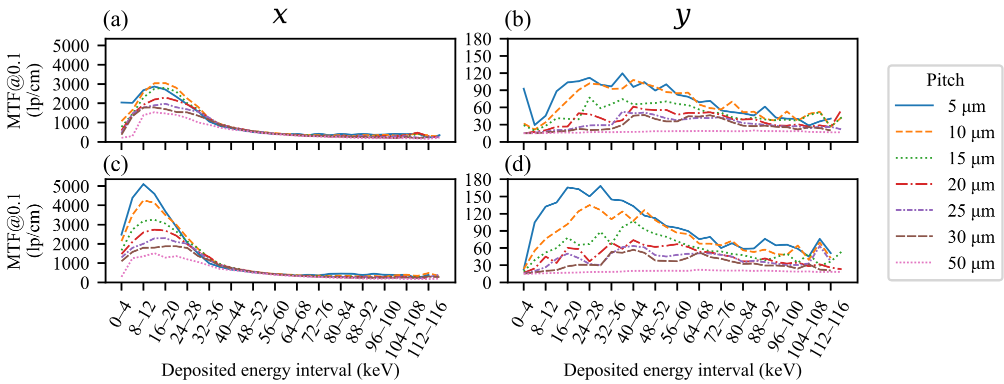

Fig. 14 For the case of eight equal-counting thresholds, panels (a)–(b) show the 10% x-MTF and y-MTF values, respectively, as a function of the true total deposited energy for the 1.5 keV lowest-threshold case. Panels (c)–(d) show the corresponding values for the 0.5 keV case.

in the higher-energy interactions, and only the 50 μm pixel pitch shows a 10% y-MTF value below 25 lp/cm, with the remaining pixel pitches well above 30 lp/cm.

Figure 14 shows that the largest improvements in both the 10% x-MTF and the 10% y-MTF occur for the lower-energy interactions when going from the 1.5 keV to the 0.5 keV case. The y-MTF also reaches a maximum at lower energies for the smaller pixel sizes, whereas the larger pixel sizes reach a maximum at higher energies. There is also a clear effect in panels (a) and (c) of Fig. 14, where the resolution has a global maximum. This maximum shifts slightly with pixel pitch but more strongly with noise level for the smaller pixel pitches. The shift with noise level suggests that lowering the noise increases the amount of usable information contained in the lower-energy interactions, thereby shifting the maximum toward lower energies. A similar effect can also be seen in the y-resolution in panels (b) and (d).

The present results were obtained for a 120 kVp spectrum after filtration by 0.8 mm Be, 4 mm Al, and 300 mm water, chosen as a representative adult-body attenuation condition. Changing the beam quality would alter the deposited-energy distribution and therefore the exact quantitative values of the reported MTFs and the optimal threshold placement. However, the main trends observed here, namely, the strong dependence on pixel pitch, the benefit of equal-counting thresholds, and the saturation with increasing threshold number, are expected to be governed primarily by the charge-sharing physics and the thresholded sampling of the charge cloud. A systematic evaluation of alternative spectra, such as 80, 100, and 140 kVp, is therefore left for future work.

Complementary to the MTF-based analysis, Fig. 15 shows the RMSE in the estimated x- and y-positions for different pixel spreads as functions of the true total deposited energy in the sensor for the 25 μm pixel pitch. For the x-resolution in panel (a), the lowest RMSE is obtained mainly for the lower-energy interactions with intermediate pixel spread, whereas both larger spreads and higher deposited energies tend to increase the uncertainty. This is also reflected in the minimum x-RMSE values, which decrease from 3.5 μm for spread 1 to 1.8 μm and 1.4 μm for spreads 2 and 3, before increasing again to 7.0 μm for spread 4. For the y-resolution in panel (b), the

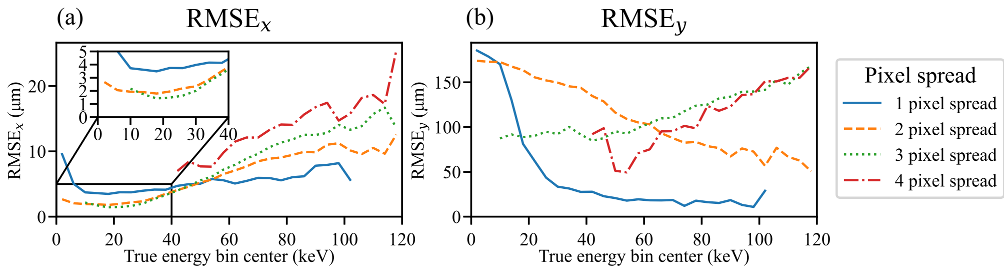

Fig. 15 (a) RMSE in the tangential direction and (b) RMSE in the wafer-thickness direction as functions of true total deposited energy bin center and pixel spread, shown for the 25 μm pixel pitch, eight equal-counting thresholds, and the 1.5 keV lowest-threshold case.

dependence is different, where the smallest spreads give the lowest RMSE at higher energies, while larger spreads show an inverted energy dependence. The minimum y-RMSE is 11 μm for spread 1, compared with 50, 85, and 49 μm for spreads 2, 3, and 4, respectively. Taken together, this shows that the information available for the x- and y-estimation is not distributed uniformly across the interaction population. This in turn suggests that a future image reconstruction could weight interactions differently based on quantities such as deposited energy and pixel spread, so that the events carrying the most useful spatial information contribute more strongly to the reconstructed image.

The achieved tangential resolution also suggests that the detector concept could be relevant for resolving interference patterns found in phase-contrast imaging, such as the previously mentioned 45 μm fringe period reported by Viermetz et al.[6] Such a fringe period corresponds to a spatial frequency of about 222.2 lp/cm, while sampling it with five points per period corresponds to a detector Nyquist frequency of about 555.6 lp/cm. Table 3 shows that even in the higher-noise case, the 10% x-MTF for the Compton interactions remains well above this value for all studied pixel sizes, ranging from 1283.7 to 2451.5 lp/cm.

4 Conclusion

In this work, we have shown that a deep-silicon edge-on sensor with thresholded event-based readout can achieve tangential resolution in the few-micrometer range, while also improving the resolution in the wafer-thickness direction. For the thresholded LUT-based reconstruction considered here, and using eight thresholds, the tangential FWHM for the Compton interactions ranged from about 1.9 to 4.9 μm in the lower-noise case and from about 3.3 to 5.1 μm in the higher-noise case, across the studied pixel pitches. For the photoelectric interactions, the corresponding tangential FWHM remained in the range 15 to 20 μm for both noise cases. This indicates that the thresholded readout can approach a spatial resolution on the order of 1 μm in the tangential direction, while the substantially coarser photoelectric resolution indicates that the electron track introduces a fundamental uncertainty.

From a CMOS design perspective, the results show that threshold flexibility is more important than simply maximizing the number of thresholds, since the achievable resolution for a given pixel pitch can be approached with a moderate number of suitably placed thresholds. Employing more than about 8 to 10 programmable thresholds gives only marginal additional improvement for the configurations studied here. At the same time, the achievable y-resolution remains fundamentally limited by the charge-cloud information available in the thresholded pixel response, with substantial improvement requiring pixel pitches below about 30 μm and the strongest gains occurring for pitches of about 20 μm and below, depending on the noise level. Taken together, the results suggest that the achievable limit of the LUT-based approach is a tangential resolution of a few micrometers for the lower-energy interactions, but only about 15 to 20 μm for higher-energy interactions, while the wafer-thickness resolution remains limited to tens to hundreds of micrometers even for the smallest pixel pitches studied. The tangential resolution achieved for the studied pixel pitches also suggests that pixel pitches in this range could be relevant for analyzer-free phase-contrast CT, where interference patterns on the order of a few tens of micrometers are expected.

Disclosures

Mats Persson discloses research support and license fees from GE HealthCare.

Code and Data Availability

The custom Allpix Squared code is available in Ref. 19, with the supporting dataset available in Ref. 22.

Acknowledgments

This research was supported by the European Union (EIC, 1MICRON, Grant No. 101186826). The authors acknowledge the use of ChatGPT (OpenAI) for proofreading and grammar correction during paper preparation. All scientific reasoning, methodological choices, verification of accuracy, and final text revisions were carried out by the authors. The computations and data handling were enabled by resources provided by the National Academic Infrastructure for Supercomputing in Sweden (NAISS), partially funded by the Swedish Research Council through Grant No. 2022-06725.

References

1. T. Corradino et al., "ARCADIA MAPS process qualification through the electrical characterization of passive pixel arrays," *J. Instrum.* **18**, C02045 (2023).
2. U. Follo et al., "First results on monolithic CMOS detector with internal gain," *J. Instrum.* **19**, P07033 (2024).
3. M. Da Rocha Rolo et al., "ARCADIA fully depleted CMOS MAPS development with LFoundry 110 nm CIS," *Front. Sens.* **6** (2025).
4. R. Brunskog et al., "First experimental evaluation of a high-resolution deep silicon photon-counting sensor," *J. Med. Imaging* **11**(1), 013503 (2024).
5. M. Bertilson et al., "Analyzer-free hard X-ray interferometry," *Phys. Med. Biol.* **69**, 045011 (2024).
6. M. Viermetz et al., "Dark-field computed tomography reaches the human scale," *Proc. Natl. Acad. Sci. U. S. A.* **119**(8), e2118799119 (2022).
7. F. Pfeiffer et al., "Phase retrieval and differential phase-contrast imaging with low-brilliance X-ray sources," *Nat. Phys.* **2**(4), 258–261 (2006).
8. F. Pfeiffer et al., "Hard-X-ray dark-field imaging using a grating interferometer," *Nat. Mater.* **7**(2), 134–137 (2008).
9. J. Haeusele et al., "Advanced phase-retrieval for stepping-free X-ray dark-field computed tomography," *IEEE Trans. Med. Imaging* **42**(10), 2876–2885 (2023).
10. M. Viermetz et al., "Technical design considerations of a human-scale Talbot-Lau interferometer for dark-field CT," *IEEE Trans. Med. Imaging* **42**(1), 220–232 (2023).
11. C. Sundberg et al., "1-μm spatial resolution in silicon photon-counting CT detectors," *J. Med. Imaging* **8**, 063501 (2021).
12. S. Cartier et al., "Micrometer-resolution imaging using MÖNCH: towards G2-less grating interferometry," *J. Synchrotron Radiat.* **23**(6), 1462–1473 (2016).
13. S. Spannagel et al., "Allpix^2: a modular simulation framework for silicon detectors," *Nucl. Instrum. Methods Phys. Res. A* **901**, 164–172 (2018).
14. G. Poludniowski et al., "Technical note: SpekPy v2.0—a software toolkit for modeling X-ray tube spectra," *Med. Phys.* **48**(7), 3630–3637 (2021).
15. R. Bujila, A. Omar, and G. Poludniowski, "A validation of SpekPy: a software toolkit for modelling X-ray tube spectra," *Phys. Med.* **75**, 44–54 (2020).
16. COSMOL AB, "COMSOL Multiphysics® v. 6.2," COMSOL AB, Stockholm (accessed 2026-02-26) (2025).
17. W. Shockley, "Currents to conductors induced by a moving point charge," *J. Appl. Phys.* **9**, 635–636 (1938).
18. S. Ramo, "Currents induced by electron motion," *Proc. IRE* **27**, 584–585 (1939).
19. G. N. Kunkler and R. Brunskog, "Custom allpix squared fork with interactivepropagation and propagation-summary," Version 1.0.1, Zenodo (2026).
20. D. Freedman and P. Diaconis, "On the histogram as a density estimator: L2 theory," *Z. Wahrscheinlichkeitstheorie Verw. Geb.* **57**, 453–476 (1981).
21. D. W. Scott, "On optimal and data-based histograms," *Biometrika* **66**, 605–610 (1979).
22. R. Brunskog et al., "Supporting dataset," Version 1, Zenodo (2026).

Rickard Brunskog graduated with an MSc degree in engineering physics from KTH Royal Institute of Technology in 2022 and is currently a PhD student in the Physics of Medical Imaging Division at KTH. His research interests involve the development of ultra-high-resolution deep silicon photon counting detectors and their use in clinical phase-contrast imaging.

Mats Persson received his PhD degree in Physics in 2016 from KTH Royal Institute of Technology in Stockholm. After spending three years as a postdoctoral researcher at Stanford University and at General Electric Research Center, he returned to KTH in 2020, where he is now an Associate Professor of Physics. His research interests are focused on image reconstruction and mathematical performance modeling for photon-counting spectral CT.

Moa Yveborg Tamm is a researcher at KTH Royal Institute of Technology with over 15 years of experience in medical imaging, silicon detector technology, and translational research.

She earned her PhD degree in Physics from KTH, focusing on photon-counting CT and silicon detectors, and has contributed to the development of novel photon-counting imaging systems from fundamental research to clinical validation. Her current research focuses on advanced imaging technologies and next-generation detector systems.

Umberto Follo is a researcher at INFN Torino working on the development of monolithic CMOS sensors for computed tomography (CT) applications. He received his M.Sc. degree in Nuclear and Subnuclear Physics from the University of Turin and recently completed his PhD degree in Electrical, Electronics, and Communications Engineering at Politecnico di Torino. His research focuses on CMOS sensor design, front-end electronics, and the characterization of semiconductor detectors.

Mats Danielsson is a professor at KTH Royal Institute of Technology and division leader in Physics of Medical Imaging, and is a co-founder of MedTechLabs (Stockholm). He received his PhD for research conducted at CERN and was a postdoc at Berkeley. His main research interest is photon counting detectors, and he has 120 publications and more than 150 approved patents. He is a co-founder of several successful start-ups, such as Sectra Mamea, C-RAD, and Prismatic Sensors.